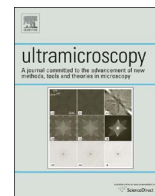




ELSEVIER

Contents lists available at ScienceDirect

Ultramicroscopy

journal homepage: www.elsevier.com/locate/ultramic

Energy-filtered environmental transmission electron microscopy for the assessment of solid–gas reactions at elevated temperature: NiO/YSZ–H₂ as a case study



Q. Jeangros^{a,b,*}, T.W. Hansen^c, J.B. Wagner^c, R.E. Dunin-Borkowski^d, C. Hébert^a, J. Van herle^e, A. Hessler-Wyser^{a,b}

^a Interdisciplinary Centre for Electron Microscopy, Ecole Polytechnique Fédérale de Lausanne, Lausanne, Switzerland

^b Photovoltaics and Thin Film Electronics Laboratory, Ecole Polytechnique Fédérale de Lausanne, Neuchâtel, Switzerland

^c Center for Electron Nanoscopy, Technical University of Denmark, Lyngby, Denmark

^d Ernst Ruska-Centre for Microscopy and Spectroscopy with Electrons and Peter Grünberg Institute, Jülich Research Centre, Jülich, Germany

^e Fuelmat Group, Ecole Polytechnique Fédérale de Lausanne, Sion, Switzerland

ARTICLE INFO

Article history:

Received 21 January 2016

Accepted 19 June 2016

Available online 22 June 2016

Keywords:

Environmental transmission electron microscopy

Energy-filtered transmission electron microscopy

Solid oxide fuel cells

Reduction

Reaction mechanisms

ABSTRACT

A novel approach, which is based on the analysis of sequences of images recorded using energy-filtered transmission electron microscopy and can be used to assess the reaction of a solid with a gas at elevated temperature, is illustrated for the reduction of a NiO/ceramic solid oxide fuel cell anode in 1.3 mbar of H₂. Three-window elemental maps and jump-ratio images of the O K edge and total inelastic mean free path images are recorded as a function of temperature and used to provide local and quantitative information about the reaction kinetics and the volume changes that result from the reaction. Under certain assumptions, the speed of progression of the reaction front in all three dimensions is obtained, thereby providing a three-dimensional understanding of the reaction.

© 2016 Elsevier B.V. All rights reserved.

1. Introduction

A comprehensive analysis of the reaction mechanisms that control how a microstructured solid reacts with a gas at elevated temperature is essential in fields ranging from catalysis to mining. Although reaction mechanisms are invariably complicated, they are usually inferred by monitoring the evolution of one parameter, such as mass, conductivity, crystallography, microstructure or composition during reaction. Furthermore, conventional techniques usually only allow one aspect of a process to be retrieved, such as microstructure or chemistry, but typically not both at the same time. Part of the description is then missing and post-exposure observations using techniques such as electron microscopy and models to data acquired *in situ* are often required. However, transient processes may not be resolved in post-exposure micrographs and models may only provide a simplified description in the form of a single reaction mechanism.

Techniques such as full-field transmission X-ray microscopy are promising as a result of their ability to capture changes in both

morphology and chemical composition at the same time, with a spatial resolution that is now in the range of a few tens of nm [1]. However, this spatial resolution may not be sufficient to resolve fine details in a reaction. In contrast, environmental transmission electron microscopy (ETEM) has the ability to obtain both structural and chemical diagnostic information on the (sub-)nm scale in a gas atmosphere at elevated temperature. The technique has been applied to a variety of problems, most of which have been related to the characterisation of catalytic nanoparticles under operating conditions, as reviewed in [2,3]. These studies have covered topics such as changes in nanoparticle size and shape [4], the nucleation of nanotubes [5], the visualisation of gas adsorption [6], reduction–oxidation cycles of nanoparticles in various atmospheres [7–12] and measurements of catalyst activity using electron energy-loss spectroscopy [13].

Sharma et al. demonstrated that either images or electron energy-loss (EEL) spectra could be used to obtain reaction kinetics in an electron microscope [14]. A sequence of images of a specimen can be used to provide local quantitative information about the progression of a reaction, e.g., by measuring the evolution of an area of dense unreacted NiO during reduction to porous Ni in H₂ [15]. However, structural changes induced by the reaction may be subtle and difficult to quantify directly from images. Changes in

* Corresponding author at: Photovoltaics and Thin Film Electronics Laboratory, Ecole Polytechnique Fédérale de Lausanne, Neuchâtel, Switzerland.

diffraction peak intensities may also provide information about the kinetics of a change in crystallography, for example from nickel oxide (NiO) to metallic Ni in H₂ or *vice versa* in O₂ [15–17]. However, diffraction peak intensities are sensitive to specimen orientation with respect to the electron beam, which may change due to thermal drift or changes in microstructure during a reaction. In addition, the technique has limited spatial resolution when using a selected area aperture. In contrast, EEL spectroscopy (EELS) provides direct chemical analysis of a sample down to the sub-nm scale. Spectra are typically acquired at different positions of the electron beam by means of scanning TEM (STEM), in order to obtain spatial information. However, the serial acquisition of spectra is challenging when performing dynamic experiments at elevated temperature as each pixel in a spectrum image corresponds to a different reaction time and the specimen may be subject to thermal drift and changes in microstructure. As a result, small numbers of EEL spectra are usually acquired at each reaction step to provide averaged chemical information about a specimen and these values are then correlated with images that contain information about changes in microstructure [16,17].

Alternatively, energy-filtered TEM (EFTEM) can be used to provide local structural and chemical information from features in an EEL spectrum through the use of an energy-selecting slit. While the quality of EFTEM images also suffers from the effect of thermal drift and changes in microstructure during image acquisition (typically on the order of a few tens of seconds for core losses), the technique offers faster elemental analysis for the same number of pixels when compared with STEM EELS. However, this speed comes at the expense of fine details in the energy-loss spectrum. For example, images filtered at plasmon losses have been used in combination with STEM EELS to assess the reaction of materials in liquids, enabling the distinction of regions with different chemistry [18]. Recently, we demonstrated that EFTEM could be applied successfully at elevated temperature in a gas atmosphere to yield local quantitative measurements of both microstructure and chemistry in a NiO/yttria-stabilised zirconia (YSZ) sample reacting in H₂ [19]. By using sequences of three-window oxygen K edge elemental maps and t/λ total inelastic mean free path images, where t is the specimen thickness and λ is the total inelastic mean free path, the evolution of the NiO fraction and corresponding volume changes could be monitored as a function of temperature.

In this paper, the objectives are to complement the previous study [19] by demonstrating that (i) jump-ratio images (here for the O K edge) can be used to provide quantitative kinetic information in a similar manner to using three-window elemental maps, (ii) a combined knowledge of chemistry and t/λ at the same position during a reaction provides valuable information about how a reaction front propagates in three dimensions from two-dimensional images and (iii) this local and quantitative information can be correlated with the mechanisms that control the reaction. As a result, a three-dimensional picture of the reaction between a gas and a solid at elevated temperature is obtained, where both the solid surface and the bulk material react with the gas.

2. Experimental details

2.1. Materials and sample preparation

Details about the sample and its preparation for TEM examination have been published elsewhere [19]. In short, TEM samples of NiO/YSZ, a standard solid oxide fuel cell anode, were prepared using a conventional focused ion beam (FIB) lift-out technique (Zeiss NVision 40) and attached onto stainless steel grids using C. Final thinning was performed at 5 kV.

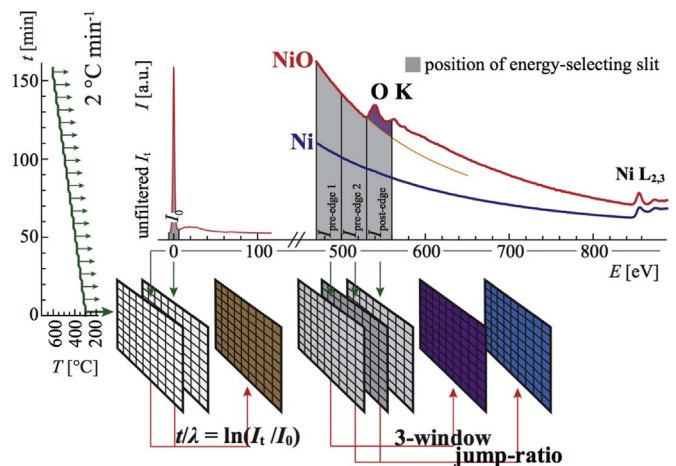


Fig. 1. Time and temperature parameters used to approximate a 2 °C min⁻¹ ramp, shown alongside the positions of the energy-selecting slit used to acquire five different images at each temperature step. EEL reference spectra recorded from the same grain at 30 °C (NiO) and after reduction in 1.3 mbar of H₂ at 604 °C (Ni), 130 min after reaching the end of the ramp, are shown.

2.2. Energy-filtered environmental TEM

The TEM lamella was mounted in a Gatan Inconel 652 double-tilt heating holder. Its reduction was studied in a differentially pumped FEI Titan E-Cell 80-300ST ETEM [20] operated at 300 kV at a constant electron dose rate of $\sim 10^3$ e⁻ nm⁻² s⁻¹.

As illustrated in Fig. 1, the evolution of different features in the EEL spectrum was followed during reduction of the thin NiO/YSZ lamella in 1.3 mbar of H₂ (at a flow rate of H₂ of 2 mL min⁻¹) at elevated temperature. A 20 μm condenser aperture was used to define a collection semi-angle β of 6.8 mrad.

Specimen thickness maps were determined from t/λ images using the log-ratio method from unfiltered I_t and zero-loss filtered I_0 images [21] acquired using an energy-selecting slit width Δ of 10 eV and an acquisition time of 0.2 s (Fig. 1). The total inelastic mean free path λ was estimated to be 155 nm for NiO from a mean energy-loss E_m of 19.8 eV reported in [22] and 127 nm for Ni by computing a value for E_m of 25.2 eV using the atomic number of Ni (28).

At higher energy-losses, the intensity in the O K ionisation edge, which was obtained from both three-window elemental maps and jump-ratio images, was used to determine the spatial distribution of O atoms. Values for Δ of 30 eV and an acquisition time of 40 s (sometimes reduced to 20 s if thermal drift was too severe) were used to acquire $I_{\text{pre-edge 1}}$ (at an energy-loss onset of 472 eV), $I_{\text{pre-edge 2}}$ (502 eV) and $I_{\text{post-edge}}$ (532 eV) images for three-window elemental mapping using the O K edge [21] (Fig. 1). As an objective aperture must be used when acquiring EFTEM images to guarantee sufficient spatial resolution [23], diffraction effects are always present to some extent and modify the intensity in the three-window maps. An alternative approach involved the division of $I_{\text{post-edge}}$ by $I_{\text{pre-edge 2}}$ images to yield O K edge jump-ratio images (Fig. 1), in which diffraction effects are reduced.

t/λ maps and O K edge three-window and jump-ratio images acquired at 30 °C in H₂ served as initial unreduced NiO/YSZ references. In addition, a three-window Ni L_{2,3} elemental map was acquired at this temperature to differentiate the YSZ grains from NiO. After a slow heating ramp up to 250 °C and then, when the sample was stable (30 min later), up to 300 °C, the temperature was increased to 604 °C in steps of 16 °C (over 2 min for each step) and t/λ maps, O K three-window and jump-ratio images were acquired during a 6 min isothermal step, before increasing the temperature again to maintain an average heating rate of 2 °C min⁻¹ (Fig. 1). The sample was left at the final temperature of

604 °C for 130 min before acquiring a final set of t/λ maps and O K three-window and jump-ratio images, which served as Ni/YSZ references, with EELS confirming full reduction of the sample.

2.3. Data processing

All of the energy-filtered images acquired in the ETEM were aligned after filtering (using a Sobel isotropic 3×3 gradient operator [24]) with the SDDS Digital Micrograph plugin [25], in order to ensure that each region remained at the same pixel coordinates (x,y) throughout the reaction.

To convert changes in intensity in the pixels belonging to the NiO phase to a volume loss (for t/λ maps) or to reduction kinetics (for O K three-window and jump-ratio images), any fluctuation in intensity between images that is not related to structure or chemistry but, e.g., to differences in acquisition time, must be removed. This was done using the YSZ phase as a reference as it is structurally and chemically stable in these reaction conditions [26]. All of the images were normalised so that the intensity measured in the pixels corresponding to YSZ remained at a mean value that is constant and specific to each sequence of t/λ , O K three-window and jump-ratio images.

These processed three-window maps and jump-ratio images were then analysed to provide details about the evolution of the number of O atoms in the NiO phase. The fraction of NiO that had converted to Ni, $\alpha(T,x,y)$, could be obtained at each temperature step T and at all pixel coordinates (x,y) . This was done by scaling the intensity $I_{O(T,\beta,\Delta,x,y)}$, which was measured in the Ni(O) phase at a temperature T and position (x,y) , using values measured in the experimental NiO and Ni references at the same (x,y) coordinates ($I_{O(NiO)}(\beta,\Delta,x,y)$ and $I_{O(Ni)}(\beta,\Delta,x,y)$, respectively; see Fig. 2)

$$\alpha(T, x, y) = \frac{I_{O(NiO)}(\beta, \Delta, x, y) - I_{O(T, \beta, \Delta, x, y)}}{I_{O(NiO)}(\beta, \Delta, x, y) - I_{O(Ni)}(\beta, \Delta, x, y)} \quad (1)$$

It should be noted that an experimental value was used for $I_{O(Ni)}(\beta,\Delta,x,y)$ instead of 0 to account for potential artefacts related to dark reference of the camera, background and diffraction effects.

As the reaction front between the newly-formed Ni phase and the initial NiO grain is sharp, without any intermediate phase [19,26], the equivalent thickness of NiO $t_{NiO}(T,x,y)$, of Ni $t_{Ni}(T,x,y)$ and of the specimen $t(T,x,y)$ could be estimated at each position (Fig. 2). If plasmonic excitations at interfaces in the structure (between voids, NiO and/or Ni) are ignored [27], it is possible to estimate, by using $\alpha(T,x,y)$ and $t/\lambda(T,x,y)$ computed at the same coordinates (x,y) and temperature T

$$t_{NiO}(T, x, y) \approx t/\lambda(T, x, y)[1 - \alpha(T, x, y)]\lambda_{NiO} \quad (2)$$

$$t_{Ni}(T, x, y) \approx t/\lambda(T, x, y)\alpha(T, x, y)\lambda_{Ni} \quad (3)$$

$$t(T, x, y) \approx t_{NiO}(T, x, y) + t_{Ni}(T, x, y). \quad (4)$$

As discussed below, this procedure allows the position of the Ni/NiO reaction front within the specimen depth (in the z direction) to be estimated, in order to provide a three-dimensional picture of the reaction.

3. Results and discussion

3.1. Spatially-localised reaction kinetics from O K edge images

A representative selection of unfiltered bright-field (BF) TEM images, t/λ and three-window O K elemental maps, acquired during reduction up to 604 °C in 1.3 mbar of H_2 , is shown in Fig. 3. An EEL reference spectrum recorded from one NiO grain at 30 °C is shown in the upper right corner. The appearance of small voids in the NiO at grain boundaries with the YSZ is indicative of activation of the reaction just below 350 °C (Fig. 3b). The voids are observed directly in the t/λ map (Fig. 3b.2) and appear as dark regions in the O elemental map (Fig. 3b.3). Reduction of NiO is initiated at interfaces with the YSZ, presumably as a result of migration of O anions from NiO across the interface to O vacancies that are inherently present in the YSZ [26]. When the temperature is increased to 428 °C, additional porous O-depleted regions appear closer to the centres of the NiO grains (Fig. 3c). At 460 °C, voids are observed across the entire Ni grains as the free surfaces reduce directly, with larger voids appearing at the initial positions of some NiO/NiO grain boundaries (arrowheads in Fig. 3d). Intra and intergranular voids become larger as the temperature is increased to 604 °C (Fig. 3e). The images that were acquired 130 min after reaching 604 °C show that a coarser reduced Ni microstructure forms as the system minimises its surface energy (Fig. 3f). An EEL spectrum recorded from an individual Ni grain just before acquiring the data shown in Fig. 3f is consistent with full reduction (lower right inset). Voids appear at the positions of some initial NiO/NiO grain boundaries (black arrowheads in Fig. 3f), while other neighbouring Ni grains remain in contact throughout the entire reaction (white arrowheads in Fig. 3f). These differences are related to the symmetry characteristics of the grain boundaries: incoherent boundaries detach during the reaction, while coherent twins remain in contact [28].

Fig. 4a shows the full sequence of three-window O K elemental maps recorded during reduction up to 604 °C. In order to reduce the effects of poor signal to noise ratio on the results, the intensity in the maps was averaged before computing the kinetics. Nine different Ni(O) regions were identified in the Ni $L_{2,3}$ elemental

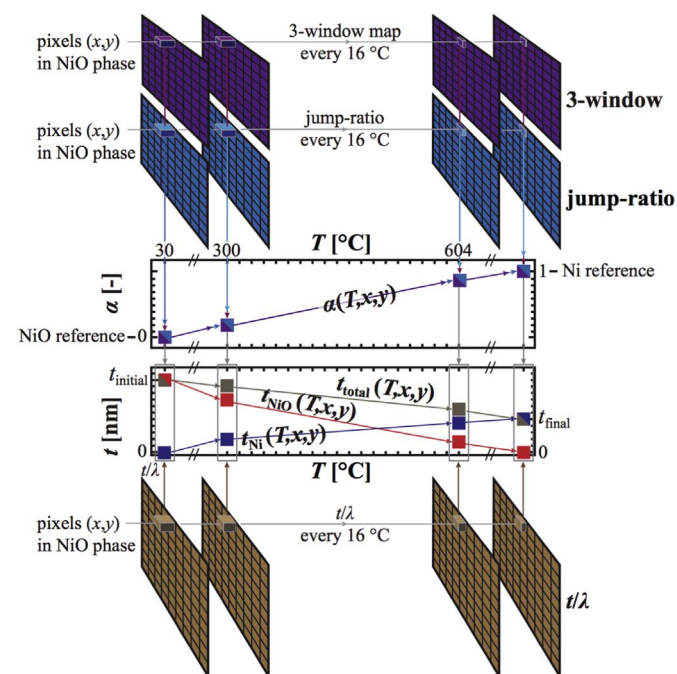


Fig. 2. Schematic diagram illustrating the methodology used in the present paper to yield (i) the conversion fraction of NiO to Ni, $\alpha(T,x,y)$, as a function of temperature T at coordinates (x,y) from a sequence of three-window elemental maps and jump-ratio images using the first (30 °C) and last (604 °C, 130 min after the end of the ramp) images as references for NiO ($\alpha=0$) and Ni ($\alpha=1$), respectively, and (ii) the evolution of the Ni, NiO and total thicknesses ($t_{Ni}(T,x,y)$, $t_{NiO}(T,x,y)$ and $t(T,x,y)$, respectively) from a combined knowledge of $\alpha(T,x,y)$ and $t/\lambda(T,x,y)$ at the same position (x,y) and temperature T .

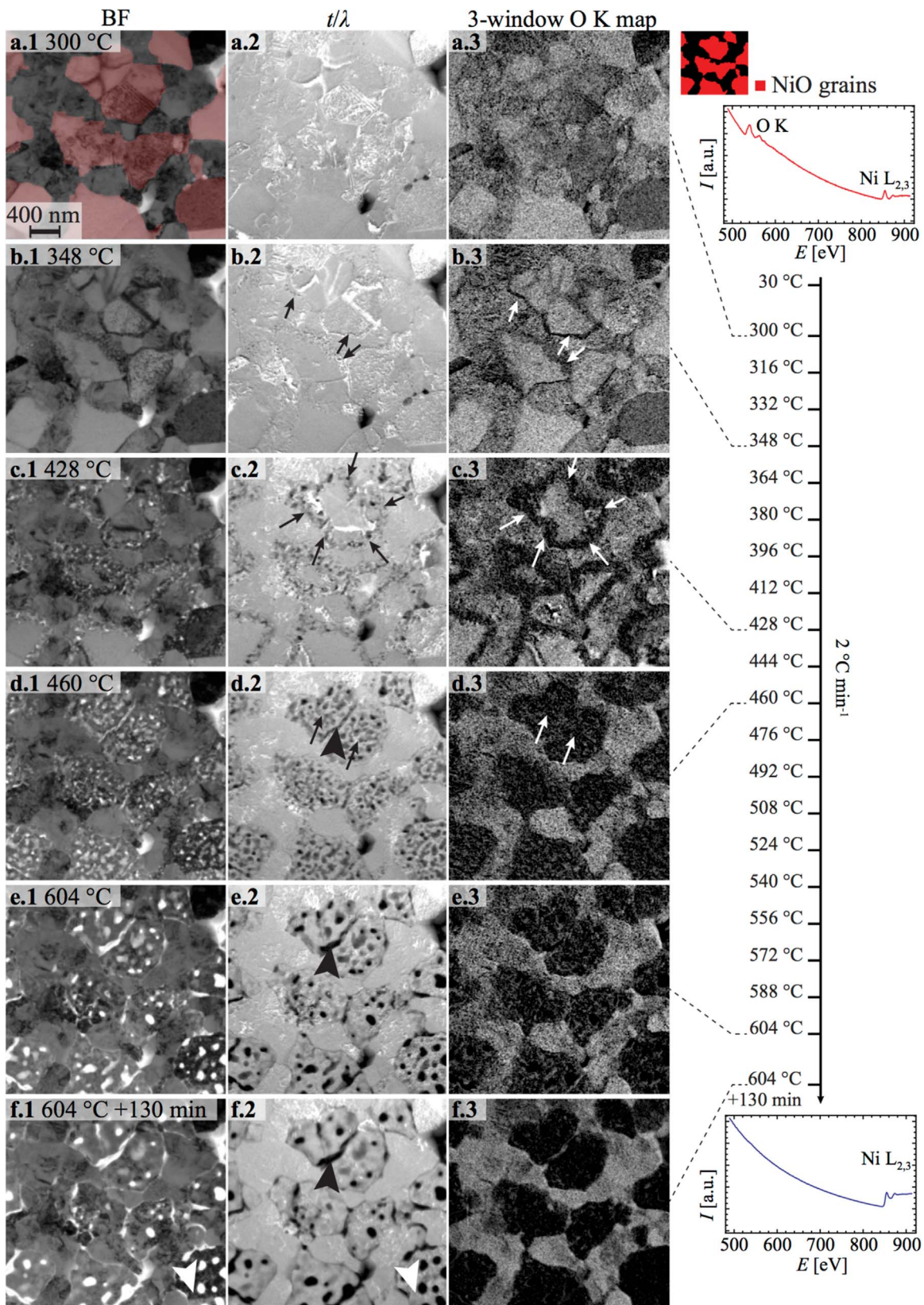
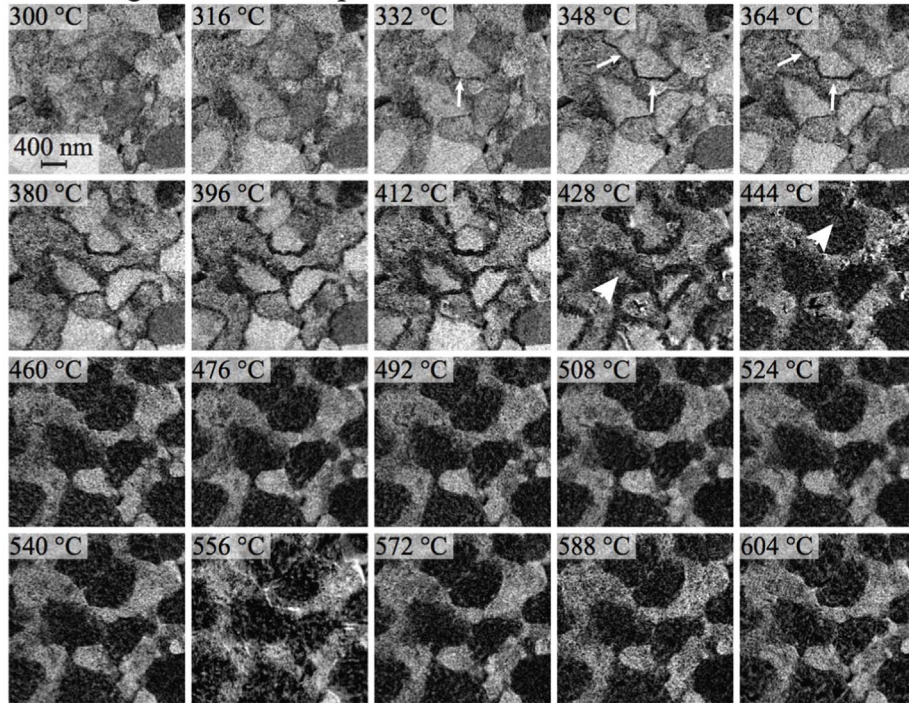


Fig. 3. (a–e) Temperature-resolved (1) BF TEM images, (2) t/λ and (3) three-window O K maps recorded during ramping at 2 °C min^{-1} in 1.3 mbar of H_2 . A red Ni EFTEM map is superimposed on (a.1) and shown as an inset (top-right corner). An EEL spectrum (lower right) confirms full reduction of the structure in (f), 130 min after reaching 604 °C . Arrows mark voids in NiO at interfaces with the YSZ in (b,c) and in the centres of grains in (d). Black arrowheads show pores at the positions of some initial NiO/NiO boundaries. White arrowheads show Ni/Ni boundaries remaining in contact in (f). (For interpretation of the references to colour in this figure legend, the reader is referred to the web version of this article.)

a O K edge elemental maps



b Reaction kinetics using O K edge elemental maps

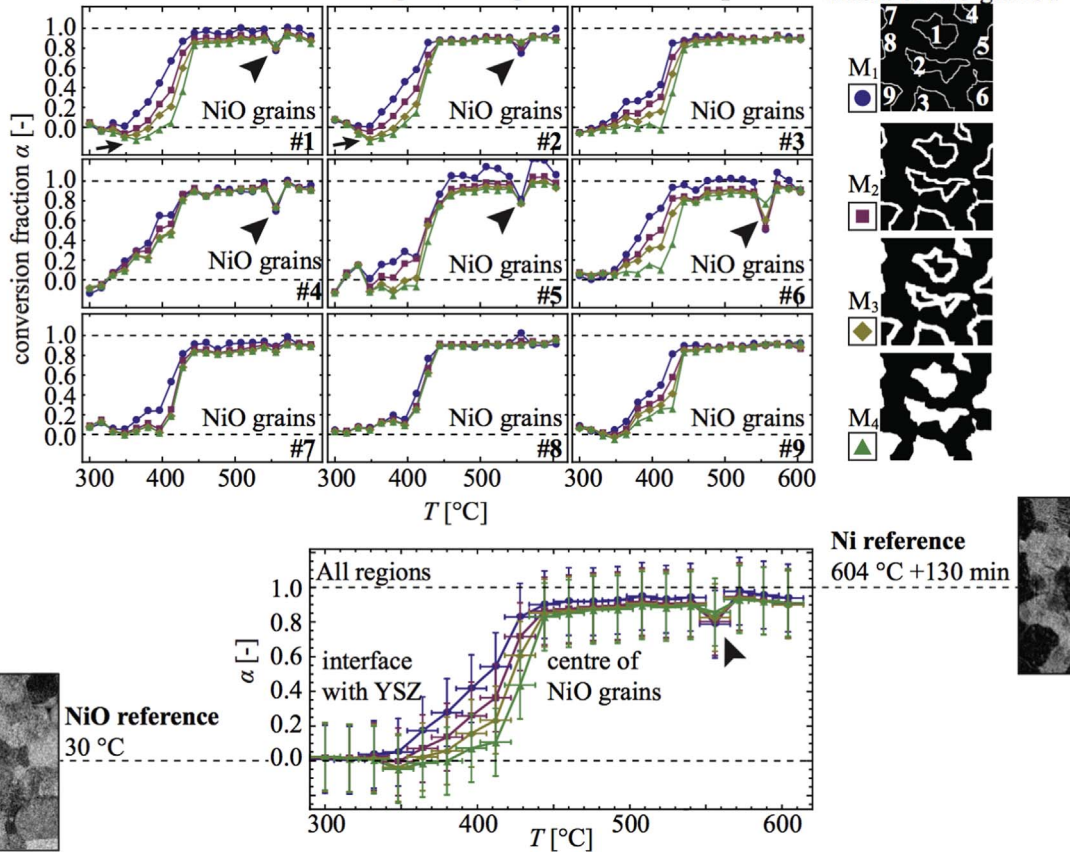


Fig. 4. (a) Three-window O K maps recorded during reduction (displayed after normalising the intensity using the YSZ phase). For each Ni(O) region identified in the Ni $L_{2,3}$ map, the average intensity in four different masks (from the YSZ interfaces, M_1 , to the entire Ni(O) grains, M_4) is scaled using the NiO and Ni reference intensities from the same regions to yield (b) the conversion fraction $\alpha(T)$. The indicated uncertainties in the determination of α are obtained using the statistical deviation when the sample is unreduced (3σ), while the horizontal uncertainties are estimated to be ± 10 °C.

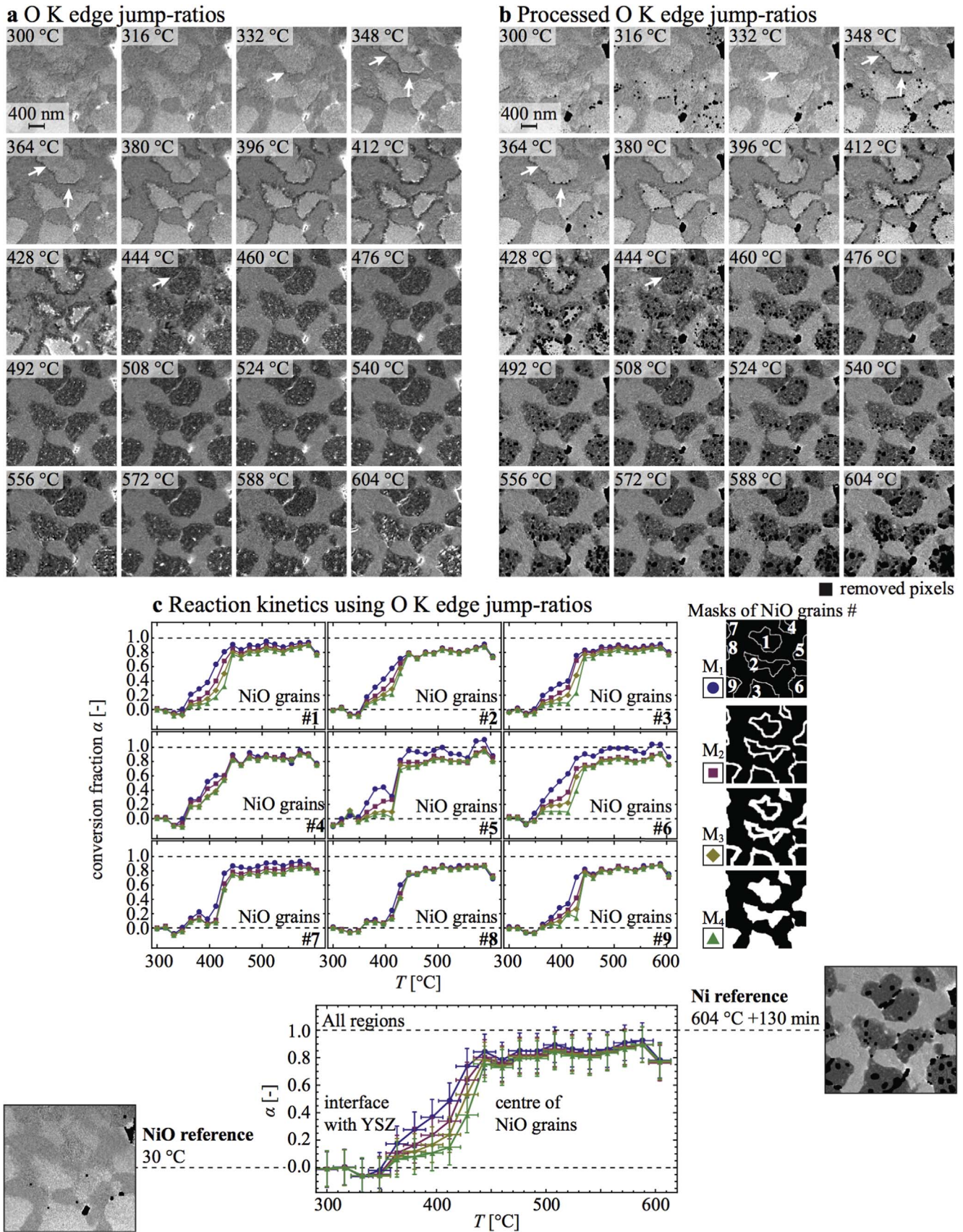


Fig. 5. (a) O K jump-ratio images (after normalisation using the YSZ phase). (b) Processed O K jump-ratio images after removal of pixels that correspond to holes or have anomalously high intensities. The average intensity in the Ni(O) regions was measured in masks M_1 to M_4 . These values were scaled using the values measured in the corresponding regions in the NiO and Ni experimental reference images to yield the reaction kinetics $\alpha(T)$ shown in (c). The uncertainties were obtained as explained in Fig. 4.

map (Fig. 4b). In each of these nine Ni(O) regions, the average intensity I_0 was measured in four different areas defined by masks M1 to M4, which were chosen to progressively select the entire Ni (O) regions starting at the interfaces with the YSZ. These values were then used to determine the conversion fraction of the reaction α by using Eq. (1) and the NiO and Ni reference intensities (Fig. 4b).

From the nine Ni(O) regions identified in the micrographs, only the regions labelled 1 and 2 are entirely within the field of view. In these regions, α is observed to increase gradually over a temperature range of 96 °C (between 348 and 444 °C) in the mask including only NiO close to the YSZ interface (upper mask M1 in Fig. 4b). In contrast, two rate-controlling mechanisms are observed to occur in succession when each group of NiO grains is analysed entirely (lower mask M4 in Fig. 4b). Indeed, α increases slowly from 348 to 412 °C due to reaction at the YSZ interface and then rapidly up to 0.9 from 412 to 444 °C as a result of free surface reduction (white arrowheads in Fig. 4a). Above 444 °C, α appears to be identical for the four different masks, demonstrating a homogeneous reaction of the Ni(O) regions. A fraction of 10% of NiO is left unreduced at the end of the heating ramp, which is consistent with previous EELS studies of the reduction of NiO particles in an ETEM [16]. The decrease in reaction rate results from the presence of H₂O, which is released by the reaction, stagnates around unreacted NiO and eventually inhibits the reaction [29]. While measurements of the reaction kinetics in regions 3–9 must be interpreted carefully since they do not show full Ni(O) regions, similar trends are observed. The apparent decrease in α at 556 °C is due to drift during acquisition (black arrowheads in Fig. 4b). The presence of bend contours (diffraction contrast) also results in an artificial decrease in α around 332–364 °C (black arrows in Fig. 4b).

Artefacts resulting from diffraction contrast are reduced when using O K jump-ratio images instead of three-window elemental maps (Fig. 5a). However, the determination of a jump-ratio image involves a division, which in turn results in the presence of pixels

with high intensities that are not related to changes in composition, especially at interfaces in the structure, as images are acquired 40 (or in some cases 20) seconds apart during the reaction. These pixels were removed by the application of a threshold, in order to infer reliable reaction kinetics from each image (Fig. 5b). The same masks M1 to M4 as in Fig. 4 were used to select different regions of the jump-ratio images. The average intensities in these regions were measured as a function of temperature (not counting pixels that were excluded by the threshold) to determine α (Fig. 5c). The results are similar to those presented in Fig. 4, even though only two energy-filtered images were used. The two reaction mechanisms (first the reaction at the YSZ interfaces and then the reaction of the free surface at higher temperature) are clearly distinguished. The total acquisition time can therefore be decreased by one third by using jump-ratio images instead of three-window elemental maps, thereby reducing the effect of drift (see data points at 556 °C in Figs. 4 and 5).

3.2. Volume changes from thickness maps

Fig. 6 shows the volume shrinkage that results from NiO reduction to Ni. The total intensity in the NiO phase measured in the initial t/λ image was compared to the total intensity in the Ni regions in the final t/λ image after multiplication by the pixel area (36 nm²) and by λ_{NiO} (155 nm) and λ_{Ni} (127 nm), respectively. An overall volume shrinkage of –41% was measured here, which is consistent with theoretical predictions of –41.6% [9]. The apparent volume shrinkage measured in each Ni(O) region varies between –36% and –46% as a result of the effects of diffraction contrast. The final values depend on the total inelastic mean free paths, the accuracy of which is estimated to be on the order of $\pm 20\%$ [22].

3.3. Reaction front dynamics

The combination of reaction kinetics and t/λ maps enables a three-dimensional analysis of the Ni/NiO reduction front. After Ni nucleation, the reaction proceeds through the progression of a reaction front as a result of the autocatalytic behaviour of the reaction: H₂ adsorbs on Ni and is transferred to the NiO in the vicinity of the reaction front, with the new Ni phase then forming at the Ni/NiO interface [29]. The speed with which this Ni/NiO reaction front propagates in the (x,y) plane can be compared with the speed with which the thickness of the sample is reducing (in the z direction). These measurements allow the assessment of whether the reaction proceeds according to different mechanisms along the free surface and in the bulk. The procedure, which is described in Fig. 7, involves the use of 3-window O K elemental maps and t/λ maps for the group of NiO grains labelled 1 in Fig. 4b. The same approach can be applied to jump-ratio images and any other NiO regions.

While the measurement of the position of the reaction front in the (x,y) plane can be performed manually, an automated procedure was chosen here, as the position of the reaction front is not always easy to identify by visual inspection. The procedure involves computation of the conversion fraction α in successive slices of the NiO phase that are 1 pixel wide using three-window O K elemental maps (Fig. 7a). Slice 1 covers the first 0–6 nm from the YSZ interface (see central inset in Fig. 7), slice 2 covers the group of pixels located 6–12 nm from the interface and so on to the centre of the NiO (slice 30, 174–180 nm from the YSZ interface).

As these 1 pixel wide regions are composed of a small number of pixels (1000 for region 1 to 140 for region 30), diffraction and noise effects are significant and affect the value of α , which takes on nonphysical values of below 0 (Fig. 7b). As diffraction contrast was mostly observed in the NiO phase, i.e., when α should be 0 but

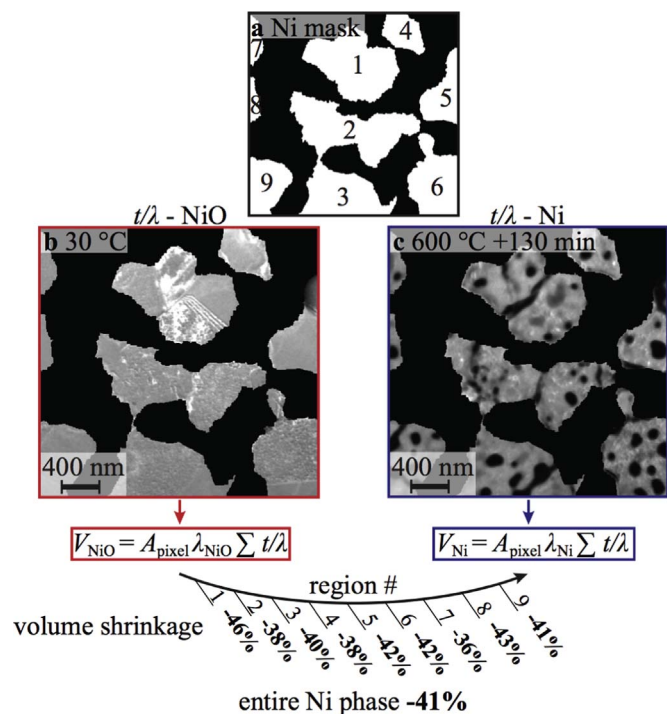


Fig. 6. Measurement of volume shrinkage. (a) Mask corresponding to the Ni phase, with 9 Ni regions labelled, which was used to segment the t/λ reference images for NiO/YSZ and Ni/YSZ to yield (b) and (c), the NiO and Ni phase before and after reduction, respectively. The volume shrinkage was obtained from (b) and (c) by using values for λ_{NiO} and λ_{Ni} (155 and 127 nm, respectively).

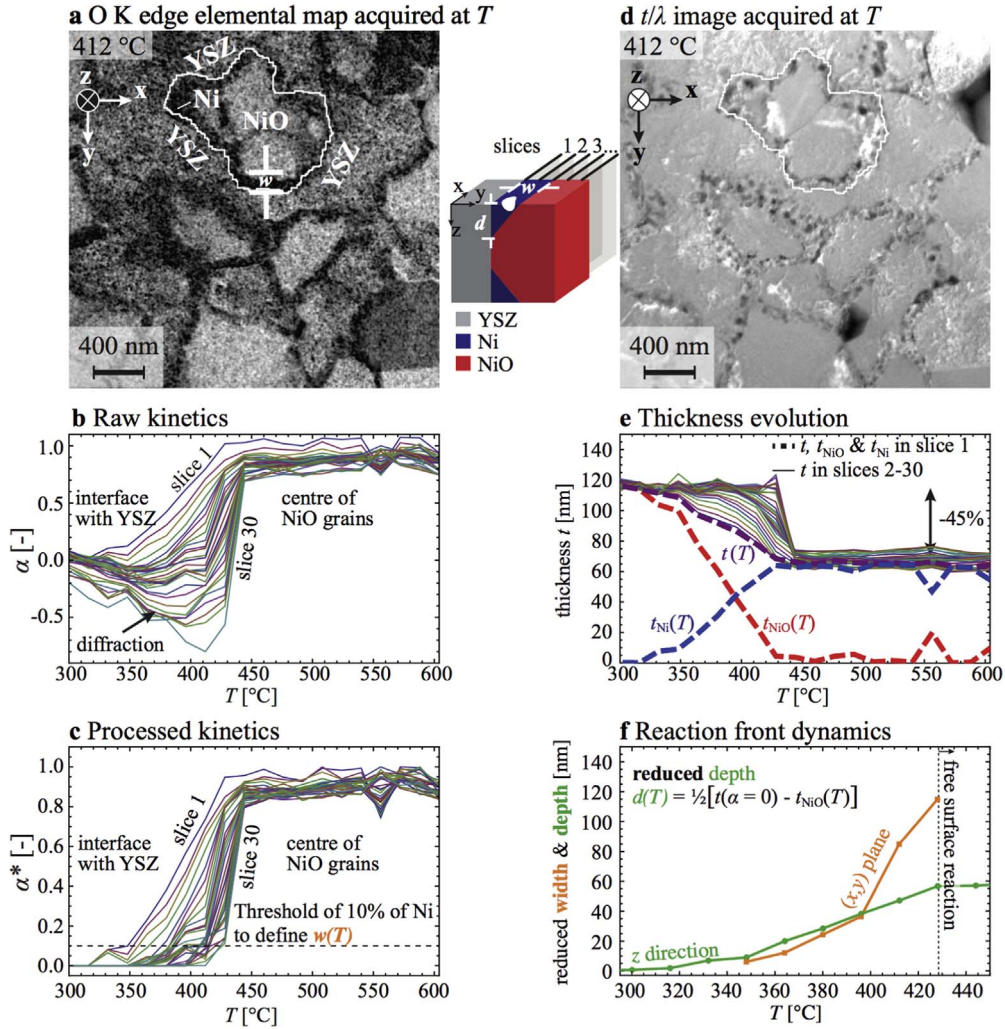


Fig. 7. (a) Three-window O K edge elemental map of the partially reduced sample at 412 °C, with one group of NiO grains highlighted (labelled 1 in Fig. 4). (b) $\alpha(T)$ in successive 1-pixel-wide regions, starting at the interface with YSZ and finishing at the centre of the group of NiO grains (see central inset), computed using Eq. (1). (c) Result of rescaling of the data between 0 and 1 and removal of data points for which $d\alpha/dT < 0$, to yield $\alpha^*(T)$. The width $w(T)$ of the reduced area is defined as the distance that encompasses all slices for which $\alpha^* \geq 0.1$ at each temperature. (d) t/λ at 412 °C, with region 1 highlighted. (e) Evolution of the total, NiO and Ni thicknesses t , t_{NiO} and t_{Ni} , respectively, for the region at the interface with the YSZ, with $t(T)$ shown for all regions. (f) Comparison of the position of the NiO/Ni reaction front in the (x,y) plane $w(T)$ and along the z axis at the YSZ interface $d(T)$.

is in fact negative (Fig. 7b), the measurements were rescaled from 0 to 1 by using the minimum and maximum values of α in each curve, while points with $d\alpha/dT < 0$ were set to 0. This procedure yielded $\alpha^*(T)$, a more physical estimate of the reaction kinetics (Fig. 7c). By using $\alpha^*(T)$, the position of the reaction front $w(T)$ in the (x,y) plane could then be estimated by determining, for each temperature, the smallest distance with respect to the YSZ interface that encompasses all of the 1-pixel-wide regions for which $\alpha^* \geq 0.1$ (Fig. 7c and f). The values of $w(T)$ that were estimated automatically using this procedure are consistent with manual measurements performed directly on the three-window O maps.

t/λ was measured in the same successive 1 pixel wide regions to assess the speed of the reaction front in the z direction, i.e., along the thickness of the sample (Fig. 7d). By using values of α^* and t/λ with Eqs. (2)–(4) for each NiO slice, estimates of the total, Ni and NiO thicknesses, $t(T)$, $t_{\text{Ni}}(T)$ and $t_{\text{NiO}}(T)$, respectively, could be computed (Fig. 7e). For clarity, $t_{\text{Ni}}(T)$ and $t_{\text{NiO}}(T)$ are only shown for the first region (1), which covers the first 6 nm of NiO from the YSZ interface, while the evolution of the total thickness $t(T)$ is shown for all successive regions (2–30, Fig. 7e). Assuming the YSZ/Ni/NiO geometry shown in the central inset of Fig. 7, the depth $d(T)$ at which the NiO/Ni reaction front is located from one of the

free surface is

$$d(T) = 1/2[t(\alpha=0) - t_{\text{NiO}}(T)]. \quad (5)$$

Estimates of the position of the NiO/Ni reaction front projected onto the (x,y) plane $w(T)$ and along the z axis at the interface with YSZ $d(T)$ are compared in Fig. 7f. $d(T)$ is compared to $w(T)$ instead of to $0.5 \cdot t_{\text{Ni}}(T)$, as both $d(T)$ and $w(T)$ include reduction-induced voids. Fig. 7f shows that the reaction rate is anisotropic, i.e., that the reaction proceeds faster along the (x,y) plane than in the z direction above 400 °C, presumably as a result of differences in the reaction mechanism in the bulk of the specimen when compared to the free surface.

3.4. NiO/YSZ reduction kinetics in H_2

Simonsen and co-workers [15] compared the reduction of NiO and NiO/YSZ fine powders in H_2 using both ETEM (through sequences of images and diffraction patterns) and thermogravimetry. They demonstrated that the YSZ phase did not inhibit Ni nucleation when mass transport of H_2 or H_2O towards and away from reaction sites was not limiting the reaction, contrary to what was initially suggested in [30]. However, the results presented in

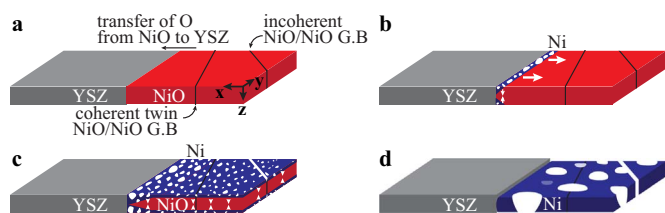


Fig. 8. Three-dimensional model of the reduction of NiO/YSZ to Ni/YSZ in 1.3 mbar of H_2 . (a) Onset of reduction due to the transfer of O anions from the NiO phase to O vacancies inherent to YSZ. (b) At ~ 350 °C, the first porous Ni domains form at interfaces with the YSZ, growing towards both the centre of the NiO grain and, at a slower rate, within the bulk. (c) At ~ 450 °C, the free surface reduces directly to metallic Ni. (d) At temperatures on the order of 600 °C, the Ni phase coarsens. Incoherent boundaries detach and leave voids, while coherent twins remain in contact during the reduction of NiO.

[15] did not show any beneficial effect of the YSZ phase on Ni nucleation, which is contrary to the present observations shown in Fig. 3. This difference may arise from the fact that NiO/YSZ was ground mechanically into a fine powder in [15], which may inhibit ionic exchanges between NiO and YSZ as interfaces are not preserved.

With regard to the reaction mechanism of NiO/YSZ with H_2 , studies have shown that either Avrami [31] or interface-controlled [32] models can describe the reaction appropriately in most cases. However, neither model appears to fully explain the present results. Indeed the reaction does not proceed through the formation of small randomly localised Ni nuclei as in the Avrami description and interface-controlled models do not take an induction time into account, as observed here in the form of an activation temperature that needs to be reached to initiate the reaction, nor substantial autocatalysis [33], two important features of the NiO reduction reaction [34].

Density functional theory calculations were used to demonstrate that O^{2-} can transfer from NiO across the NiO/YSZ interface to fill oxygen vacancies that are inherent to the YSZ phase (Fig. 8a) [26], with these O anions then desorbing as H_2O at the surface after reaction with H_2 [35]. As a result, oxygen vacancies are injected into the NiO and these sites (O^{2-} vacancies surrounded by Ni^{2+}) have been shown to act as preferential H_2 dissociation sites, with adsorbed H desorbing as H_2O and NiO reducing to Ni [36]. Once Ni domains of sufficient size have formed by this process, the reaction is expected to proceed autocatalytically through the adsorption and dissociation of H_2 directly on Ni clusters, with adsorbed H then transferring to neighbouring oxygen sites [29]. New Ni domains then form at the Ni/NiO interface and a reaction front moves towards the centre of the NiO grains, leaving a porous Ni structure behind it, as illustrated in Fig. 8b. The slower propagation rate of the reaction front through the depth of the specimen, when compared with that in the specimen plane (Fig. 7), is suggestive of a different rate-controlling mechanism below the surface. As demonstrated in [37], NiO that is located in the bulk may reduce primarily by the transfer of some of its O^{2-} to vacancies that are inherent to YSZ and not as a result of direct contact with H_2 . Above 450 °C, a sufficient number of oxygen vacancies should be present on the surface of the NiO grain, as the direct reduction of the free surface is triggered [36], with this process converting most of the bulk NiO to Ni (Fig. 8c). At this stage of the reaction, pores appear at incoherent grain boundaries, while coherent Ni twin boundaries are left intact (Fig. 8c [28]). H_2O/H_2 diffusional effects then only limit the final part of the reaction of the thin lamella in the ETEM. At the end of the reaction, porous Ni grains are observed to coarsen at temperatures on the order of 600 °C (Fig. 8d).

3.5. Factors affecting EFTEM results

In situ TEM experiments can be affected by a variety of different artefacts. FIB sample preparation can cause Ga implantation, surface damage and amorphisation, which can modify the absorption of a reactive gas. A low final milling voltage in the FIB (here 5 kV) and the high temperatures involved in the experiment may reduce surface damage. The Ga content in the present specimen was measured to be initially at an average value of 0.2 wt%, concentrated mostly around as-sintered porosity, in regions that were observed to react in a similar way to other regions. While such effects are difficult to quantify, there are no adequate alternative techniques that can be used to maintain the microstructure and to facilitate the preparation of a sample that has a constant thickness, both requirements being essential for quantitative EFTEM analysis.

The temperature measured by the thermocouple of the heating holder overestimates the true temperature at the position of the thin lamella [38,39]. This difference is influenced by the gas atmosphere and the conductivity of the support. Based on a comparison of the reduction kinetics of NiO particles measured using both EELS in the ETEM (in 1.3 mbar of H_2 at 2 °C min^{-1}) and *in situ* X-ray diffraction (in 13 mbar of H_2 at 2 °C min^{-1}), the difference was shown to be < 30 °C. Thermal drift also limits the spatial resolution of recorded images, especially when three images must be acquired in order to compute an elemental map. In this regard, recent advances in MEMS-based heating holders that are compatible with FIB-prepared samples should significantly improve the quality of EFTEM images acquired at high temperature in the future.

Electron-beam-induced artefacts can also affect observations [40–42]. The present reaction was observed to proceed faster in regions that were irradiated with a focused probe. Such an effect may be caused by local heating due to the electron beam, by knock-on damage of O (which may in turn create active sites for H_2 adsorption and dissociation [36]) and/or ionisation by the electron beam of the molecular hydrogen gas (which modifies its adsorption energy). Although operating the microscope at a low electron dose can reduce these effects, a sufficient signal is still required to obtain statistically relevant data within the desired acquisition time, especially when acquiring core-loss EFTEM images. The acquisition of EFTEM images, while the sample reacts at elevated temperature, is hence not suited to the study of electron-beam-sensitive materials that react quickly (which was not the case here). In addition, the effect of electrostatic charging induced by the electron beam, especially at interfaces, remains unclear.

However, similar porous Ni/YSZ structures could be observed under different conditions: (i) in the present study (Fig. 3), (ii) in thin FIB windows that were not irradiated by electrons but yet underwent a similar reaction in the ETEM (not shown here), (iii) in a similar study in which the reduction of NiO/YSZ that had been ground into a fine powder was studied *in situ* in the ETEM [15] and (iv) in post-exposure micrographs recorded after *ex situ* reduction of a bulk anode [43,44]. These similarities suggest that the processes observed *in situ* are representative as they result in the same microstructure. Moreover, complex Ni(O)/YSZ interactions have also been reported both experimentally and theoretically in the literature [35,37,45–47], supporting *in situ* observations and underlining the activation of the reaction at NiO/YSZ interfaces in certain reaction conditions.

Data processing can also introduce errors. Misalignment of filtered images may lead to artefacts, as the same region may not be located at the same (x,y) position throughout an EFTEM series. As the intensity is averaged over regions of 100 pixels or more to yield statistically relevant data, this effect did not appear to be significant here. Diffraction contrast modifies the intensity in

EFTEM images and in turn changes local measurements of thickness and reduction kinetics. While jump-ratio images are less sensitive to this effect, the removal of artefacts related to the division procedure may be subjective.

4. Conclusions

In this article, the possibilities of using energy-filtered environmental TEM to assess the reaction between a solid and a gas at high temperature are investigated through the study of the reduction of NiO/YSZ with H₂ up to 604 °C. Temperature-resolved energy-filtered images are used to provide quantitative information, on the pixel scale, about both the reduction kinetics of NiO to Ni and the evolution of the thickness of the reactant NiO and the product Ni. The method proposed here relies on the use of reference images for both the initial and the final state to yield the local reaction kinetics from changes in O K edge intensity, from either three-window maps or jump-ratio images. The presence of pixels in each image whose intensity does not change over the entire reaction (here the YSZ phase) is essential to remove variations in intensity that are not related to structure and/or chemistry. Total inelastic mean free path images are used to obtain experimental values of NiO and Ni thickness change and hence volume shrinkage, which are close to theoretical predictions. Local differences in reaction rate, which depend on position in the specimen (either at NiO interfaces with YSZ or in the NiO grains) or on the propagation direction of the reaction front (along the specimen free surface or in the bulk) could be estimated under certain assumptions, to provide a three-dimensional picture of the gas–solid reaction. Limitations and potential artefacts were discussed. Based on these results, a qualitative description linking the observations to different rate-controlling mechanisms is proposed for NiO/YSZ reduction in H₂.

Acknowledgements

Support is gratefully acknowledged from the Swiss National Science Foundation (Project 200021_130124 "IN Situ TEM study of reduction and oxidation of Ni(O)-ceramic composite (IN-SITE)"), the Project Roxsolidcell, as well as from the European Union Seventh Framework Programme under Grant Agreement 312483 – ESTEEM2 (Integrated Infrastructure Initiative – I3). The A.P. Møller and Chastine Mc-Kinney Møller Foundation is gratefully acknowledged for its contribution towards the establishment of the Center for Electron Nanoscopy in the Technical University of Denmark. The authors wish to thank A.B. Aebersold, D. Laub, G. Lucas, D.T.L. Alexander, M. Cantoni, F. Bobard, E. Oveisi, P. Stadelmann, Z. Wuillemin and D. Montinaro.

References

- [1] A.M. Kiss, et al., In-situ observation of nickel oxidation using synchrotron based full-field transmission X-ray microscopy, *Appl. Phys. Lett.* 102 (5) (2013) 053902–053904.
- [2] J.R. Jinschek, Advances in the environmental transmission electron microscope (ETEM) for nanoscale in situ studies of gas–solid interactions, *Chem. Commun.* 50 (21) (2014) 2696–2706.
- [3] P.A. Crozier, T.W. Hansen, In situ and operando transmission electron microscopy of catalytic materials, *MRS Bull.* 40 (1) (2015) 38–45.
- [4] P.L. Hansen, et al., Atom-resolved imaging of dynamic shape changes in supported copper nanocrystals, *Science* 295 (5562) (2002) 2053–2055.
- [5] S. Hofmann, et al., Ledge-flow-controlled catalyst interface dynamics during Si nanowire growth, *Nat. Mater.* 7 (5) (2008) 372–375.
- [6] H. Yoshida, et al., Visualizing gas molecules interacting with supported nanoparticulate catalysts at reaction conditions, *Science* 335 (6066) (2012) 317–319.
- [7] R. Sharma, et al., Observation of dynamic nanostructural and nanochemical changes in ceria-based catalysts during in-situ reduction, *Philos. Mag.* 84 (25–26) (2004) 2731–2747.
- [8] P.A. Crozier, R. Wang, R. Sharma, In situ environmental TEM studies of dynamic changes in cerium-based oxides nanoparticles during redox processes, *Ultramicroscopy* 108 (11) (2008) 1432–1440.
- [9] R. Wang, P.A. Crozier, R. Sharma, Nanoscale compositional and structural evolution in ceria zirconia during cyclic redox treatments, *J. Mater. Chem.* 20 (35) (2010) 7497–7505.
- [10] S. Chenna, R. Banerjee, P.A. Crozier, Atomic-scale observation of the Ni activation process for partial oxidation of methane using in situ environmental TEM, *ChemCatChem* 3 (6) (2011) 1051–1059.
- [11] J. Ciston, et al., Morphological and structural changes during the reduction and reoxidation of CuO/CeO₂ and Ce_{1-x}Cu_xO₂ nanocatalysts: in situ studies with environmental TEM, XRD, and XAS, *J. Phys. Chem. C* 115 (28) (2011) 13851–13859.
- [12] V. Sharma, et al., Direct observation of hydrogen spillover in Ni-loaded Pr-doped ceria, *Catal. Today* 180 (1) (2012) 2–8.
- [13] B.K. Miller, P.A. Crozier, Analysis of catalytic gas products using electron energy-loss spectroscopy and residual gas analysis for operando transmission electron microscopy, *Microsc. Microanal.* 20 (3) (2014) 815–824.
- [14] R. Sharma, Kinetic measurements from in situ TEM observations, *Microsc. Res. Tech.* 72 (3) (2009) 144–152.
- [15] S.B. Simonsen, et al., Environmental TEM study of the dynamic nanoscaled morphology of NiO/YSZ during reduction, *Appl. Catal. A: General* 489 (2015) 147–154.
- [16] Q. Jeangros, et al., Reduction of nickel oxide particles by hydrogen studied in an environmental TEM, *J. Mater. Sci.* 48 (7) (2013) 2893–2907.
- [17] Q. Jeangros, et al., Oxidation mechanism of nickel particles studied in an environmental transmission electron microscope, *Acta Mater.* 67 (2014) 363–372.
- [18] M.E. Holtz, et al., In situ electron energy-loss spectroscopy in liquids, *Microsc. Microanal.* 19 (4) (2013) 1027–1035.
- [19] Q. Jeangros, et al., Measurements of local chemistry and structure in Ni(O)–YSZ composites during reduction using energy-filtered environmental TEM, *Chem. Commun.* 50 (15) (2014) 1808–1810.
- [20] T.W. Hansen, et al., The titan environmental transmission electron microscope: specifications, considerations and first results, *Microsc. Microanal.* 15 (Suppl. 2) (2009) S714–S715.
- [21] R.F. Egerton, *Electron Energy-Loss Spectroscopy in the Electron Microscope*, Springer, New York, 2011.
- [22] T. Malis, S.C. Cheng, R.F. Egerton, EELS log-ratio technique for specimen-thickness measurement in the TEM, *J. Electron Microsc. Tech.* 8 (2) (1988) 193–200.
- [23] F. Hofer, P. Warbichler, Elemental mapping using energy filtered imaging, *Transmission Electron Energy Loss Spectrometry in Materials Science and the EELS Atlas*, Wiley-VCH Verlag GmbH & Co. KGaA 2005, pp. 159–222.
- [24] I. Sobel, A 3x3 isotropic gradient operator for image processing, *Stanford Artificial Intelligence Project (SAIL)*, (1968) 1–5.
- [25] B. Schaffer, W. Grogger, G. Kothleitner, Automated spatial drift correction for EFTEM image series, *Ultramicroscopy* 102 (1) (2004) 27–36.
- [26] Q. Jeangros, et al., In situ redox cycle of a nickel–YSZ fuel cell anode in an environmental transmission electron microscope, *Acta Mater.* 58 (14) (2010) 4578–4589.
- [27] N. Jiang, D. Su, J.C.H. Spence, On the measurement of thickness in nanoporous materials by EELS, *Ultramicroscopy* 111 (1) (2010) 62–65.
- [28] Q. Jeangros, et al., A TEM study of Ni interfaces formed during activation of SOFC anodes in H₂: influence of grain boundary symmetry and segregation of impurities, *Acta Mater.* 103C (2016) 442–447.
- [29] J.T. Richardson, R. Scates, M.V. Twigg, X-ray diffraction study of nickel oxide reduction by hydrogen, *Appl. Catal. A: Gen.* 246 (1) (2003) 137–150.
- [30] D. Fouquet, et al., Kinetics of oxidation and reduction of Ni/YSZ cermets, *Ionics* 1862–0760 (2002) 103–108.
- [31] M. Pihlatie, A. Kaiser, M. Mogensen, Redox stability of SOFC: thermal analysis of Ni–YSZ composites, *Solid State Ion.* 180 (17–19) (2009) 1100–1112.
- [32] N.M. Tikekar, T.J. Armstrong, A.V. Virkar, Reduction and reoxidation kinetics of nickel-based SOFC anodes, *J. Electrochem. Soc.* 153 (4) (2006).
- [33] H.H. Kung, *Transition Metal Oxides: Surface Chemistry and Catalysis*, Elsevier, New York, 1989.
- [34] R.P. Furstenuau, G. McDougall, M.A. Langell, Initial stages of hydrogen reduction of NiO(100), *Surf. Sci.* 150 (1) (1985) 55–79.
- [35] M. Shishkin, T. Ziegler, The oxidation of H₂ and CH₄ on an oxygen-enriched yttria-stabilized zirconia surface: a theoretical study based on density functional theory, *J. Phys. Chem. C* 112 (49) (2008) 19662–19669.
- [36] J.A. Rodriguez, et al., Experimental and theoretical studies on the reaction of H₂ with NiO: role of O vacancies and mechanism for oxide reduction, *J. Am. Chem. Soc.* 124 (2) (2002) 346–354.
- [37] B. Bonvalot-Dubois, et al., Reduction of NiO platelets in a NiO/ZrO₂/(CaO) directional composite, *J. Am. Ceram. Soc.* 71 (4) (1988) 296–301.
- [38] P. Mølgaard Mortensen, et al., Modeling of temperature profiles in an environmental transmission electron microscope using computational fluid dynamics, *Ultramicroscopy* 152 (2015) 1–9.
- [39] M. Picher, et al., Vibrational and optical spectroscopies integrated with environmental transmission electron microscopy, *Ultramicroscopy* 150 (2015) 10–15.
- [40] M.I. Buckett, L.D. Marks, Electron irradiation damage in NiO, *Surf. Sci.* 232 (3)

- (2010) 353–366.
- [41] M.I. Buckett, et al., Electron irradiation damage in oxides, *Ultramicroscopy* 29 (1–4) (1989) 217–227.
- [42] R.F. Egerton, P. Li, M. Malac, Radiation damage in the TEM and SEM, *Micron* 35 (6) (2004) 399–409.
- [43] A. Faes, et al., Design of experiment approach applied to reducing and oxidizing tolerance of anode supported solid oxide fuel cell. Part II: electrical, electrochemical and microstructural characterization of tape-cast cells, *J. Power Sources* 196 (21) (2011) 8909–8917.
- [44] M. Andrzejczuk, et al., Microstructural changes in NiO–ScSZ composite following reduction processes in pure and diluted hydrogen, *Mater. Charact.* 87 (2014) 159–165.
- [45] E.C. Dickey, et al., Structure and bonding at Ni–ZrO₂ (cubic) interfaces formed by the reduction of a NiO–ZrO₂ (cubic) composite, *Microsc. Microanal.* 3 (5) (1997) 443–450.
- [46] M. Shishkin, T. Ziegler, Oxidation of H₂, CH₄, and CO molecules at the interface between nickel and yttria-stabilized zirconia: a theoretical study based on DFT, *J. Phys. Chem. C* 113 (52) (2009) 21667–21678.
- [47] M. Shishkin, T. Ziegler, Hydrogen oxidation at the Ni/yttria-stabilized zirconia interface: a study based on density functional theory, *J. Phys. Chem. C* 114 (25) (2010) 11209–11214.